

This is the accepted manuscript made available via CHORUS. The article has been published as:

Ab initio based empirical potential applied to tungsten at high pressure

Robert C. Ehemann, Jeremy W. Nicklas, Hyounghi Park, and John W. Wilkins

Phys. Rev. B **95**, 184101 — Published 1 May 2017

DOI: [10.1103/PhysRevB.95.184101](https://doi.org/10.1103/PhysRevB.95.184101)

Ab initio based empirical potential applied to tungsten at high pressure

Robert C. Ehemann¹, Jeremy W. Nicklas², Hyoungki Park¹, and John W. Wilkins¹

¹ Department of Physics, The Ohio State University, Columbus, Ohio 43210, USA and

² The Ohio Supercomputer Center, Columbus, Ohio 43212, USA

(Dated: April 7, 2017)

Density-functional theory forces, stresses and energies comprise a database from which the optimal parameters of a spline-based empirical potential combining Stillinger-Weber and modified embedded-atom forms are determined. Accuracy of the potential is demonstrated by calculations of ideal shear, stacking fault, vacancy migration, elastic constants and phonons all between 0 and 100 GPa. Consistency with existing models and experiments is demonstrated by predictions of screw dislocation core structure and deformation twinning in a tungsten nanorod. Lastly, the potential is used to study the stabilization of fcc tungsten at high pressure.

PACS numbers: 34.20.Cf, 62.20.-x, 62.25.-g, 63.70.+h

Keywords: Interatomic potentials, tungsten, dislocation core, deformation twinning

I. INTRODUCTION

Tungsten is an exceptional transition metal exhibiting the highest tensile strength, melting point, and elastic modulus of any pure metal and has important applications in aerospace, energy and armament industries. Much interest has been focused on α -W (bcc) and β -W (A15) nanostructures including nanorods¹⁻³, nanoparticles⁴⁻⁷, and thin films⁸⁻¹⁰. Due to the technological importance of tungsten, classical interatomic potentials of various forms have been developed to study this metal¹¹⁻¹⁸.

Classical potentials – popular for their favorable scaling compared to first-principles methods – were traditionally developed by choosing analytic functional forms with a handful of free parameters determined by fitting directly to experimental bulk data such as cohesive energy, lattice and elastic constants. The force-matching method of Ercolessi and Adams¹⁹ has facilitated the development of interatomic potentials based on *ab initio* calculations of relaxed crystallographic defects, metastable structures and other non-equilibrium configurations. However, many such potentials still possess a small number of free parameters and analytic functional forms which limit their transferability, requiring researchers to take great caution in choosing a potential suitable for their region of interest. It is thus desirable to produce a single potential which can be employed to study the range of materials physics, here in tungsten.

To meet this challenge we develop a unique semi-empirical potential based on a robust database of *ab initio* calculations that samples much of the potential-energy landscape. Our model combines the Stillinger-Weber (SW)²⁰ form with the modified embedded atom method²¹ (MEAM) form with functions parameterized by quintic splines. Section II describes the functional form of the model, the density-functional theory (DFT) calculations comprising the large fitting database, and the genetic algorithm optimization scheme. Accuracy of the fitted potential is demonstrated in Section III by comparing MEAM to DFT for the various struc-

tural and elastic properties to which it was fit. Given that the potential is fit directly to important crystallographic defects, structural properties and elastic constants, transferability is demonstrated in Section IV by examining MEAM predictions for $\frac{1}{2}\langle 111 \rangle$ screw dislocation core structure, deformation twinning and detwinning of a nanorod, and dynamics of bcc and fcc tungsten at high pressure. Conclusions are given in Section V.

II. OPTIMIZATION OF THE EMPIRICAL POTENTIAL WITH FIRST-PRINCIPLES CALCULATIONS

We present a spline-based empirical potential fit to a large database of highly-converged density functional theory (DFT) calculations using a global optimization scheme based on an evolutionary algorithm.

A. Empirical extension of the MEAM potential

The embedded-atom (EAM)^{21,22} and MEAM^{12,23,24} methods have been applied to many systems including semiconductors²¹⁻²⁶ and transition metals^{12,27-30}. The original MEAM formalism involves a parametrized analytical functional form which accounts for bond-bending through angular functions with explicit *s*-, *p*-, *d*- and *f*-orbital characteristics. Lenosky *et al.*²⁵ first parametrized the MEAM formalism through the use of cubic splines for the study of defects in Si. The use of splines for parameterizing empirical potentials increases model flexibility and efficiency, and has been successfully applied to the study of martensitic transformations in pure titanium²⁸, shock-loading in niobium^{29,31} and dislocation dynamics in molybdenum³⁰. SW potentials, initially developed for the modeling of cubic-diamond Si, have been successfully applied to amorphous Si³² as well as Ge³³ and other systems.

Model flexibility is paramount when constructing empirical potentials. The addition of distinct terms to the model can improve flexibility, as demonstrated by the

success of MEAM over EAM^{34,35}. However, care must be taken when parameters are added to ensure that one is not over-fitting the database and added functions should in general have a physical interpretation. Without careful balance of database inputs and model flexibility, a potential can have a low fitting error with little physical meaning or a large fitting error with little practical use.

In the present work, we propose an empirical extension of MEAM which includes a SW-type three-body term in the energy. Our model employs functions parameterized by quintic splines which improve performance for properties requiring continuous third derivatives of the interatomic potential, e.g. C_{ij} vs. P relations, over cubic splines. The total potential energy is that of SW with the addition of an embedding term U ,

$$V_{tot} = \sum_{i>j} \phi(r_{ij}) + \sum_i U(n_i) + \sum_{\substack{i,j>k \\ j \neq i}} p(r_{ij})p(r_{ik})q(\cos \theta_{jik}), \quad (1)$$

where the “electronic density” n_i at atom i involves two- and three-body contributions

$$n_i = \sum_{j \neq i} \rho(r_{ij}) + \sum_{\substack{j>k \\ j \neq i}} f(r_{ij})f(r_{ik})g(\cos \theta_{jik}), \quad (2)$$

and θ_{jik} is the angle of the triplet centered on atom i . This is the simplest extension of MEAM which does not include four-body terms and cannot be gauge-transformed back to the original model. It contains as special cases the SW ($U = 0$), MEAM ($q = 0$), and EAM ($g = q = 0$) forms. This flexibility gives us the ability to fit to a large ab-initio database described in the next section.

B. Density-functional theory database

DFT calculations performed with VASP^{36–39} using a projector-augmented plane-wave basis⁴⁰ and Perdew-Burke-Erzenhof (PAW-PBE)^{41,42} generalized-gradient exchange correlation approximation comprise a database of forces, stresses and energies for fitting via the force-matching method. In addition to $6s$ and $5d$, the $5p$ electrons are treated as valence to improve accuracy at high pressures, where the overlap of these semi-core states is not necessarily negligible. A plane-wave energy cutoff of 600 eV and first-order Methfessel-Paxton smearing width of 0.1 eV are used for all calculations; k-points are sampled on a Γ -centered $40 \times 40 \times 40$ mesh in the bcc brillouin zone. These quantities are chosen to ensure convergence of the total energy to within 0.1 meV/atom. Additional computational details are presented in Fellinger⁴³.

The *ab-initio* fitting database contains 596 configurations with a total 14,690 unique force components,

stress components and energies to be fit. The potential contains 194 fitted parameters.

Configurations in the database include volumetric strains of bcc, fcc, hcp, β -W (A15), β -Ta (β -U) and ω -Ti. Tetragonal strains are included for hcp and ω -Ti structures to ensure accurate c/a values. The database also contains elastic constants of the bcc phase at pressures between 0 and 100 GPa, in increments of 25 GPa, using volume-conserving orthorhombic and monoclinic strains of 0.5 % for $C' = \frac{1}{2}(C_{11} - C_{12})$ and C_{44} , respectively. At zero pressure, configurations with orthorhombic strains up to 10 % and monoclinic strains up to 40 % are added. Unrelaxed symmetry-inequivalent configurations of $\langle 110 \rangle$ and $\langle 112 \rangle$ γ -surfaces, ideal shear strain and vacancy migration are included at five equally spaced pressures between 0 and 100 GPa. Relaxed zero-pressure structures containing a vacancy at the lattice site and halfway along the $\langle 111 \rangle$ migration path are also added. A $7 \times 7 \times 7$ bcc supercell with a single atom displaced by 0.006 Å is included to promote accurate force-constants and phonons via the small-displacement method^{44,45}. Using a supercell of this size reduces the interaction of the displaced atom with its images across periodic boundaries and thus improves the accuracy of calculated force-constants and phonon dispersions. Relaxed low-index free surfaces as well as crowdion, octahedral, $\langle 111 \rangle$ -split and $\langle 110 \rangle$ -split self-interstitial configurations are included. *Ab-initio* MD snapshots of 125-atom bcc supercells at 1620 K, 2960 K and a liquid tungsten at 6730 K are added to improve performance for simulations at high temperature. A 36-atom hcp supercell at 100 K is also included. Lastly, a mesh of 36 points on the Bain⁴⁶ (bcc-fcc) and Burgers⁴⁷ (bcc-hcp) energy surfaces at pressures of 0 GPa and 700 GPa in addition to 600 GPa for the Bain path and 800 GPa for the Burgers path are included to ensure that the potential can be used to explore properties of these close-packed phases at high pressure.

C. Genetic algorithm optimization

Development of the optimized potential is an iterative process of fitting, testing and database refinement. Ten to twenty fits are performed simultaneously and the resultant potentials are tested for accuracy on a range of properties. The fitting database is refined based on the results of these tests: new structures are added to correct spurious behavior or structures are removed when under-fitting is suspected. For example, points on the Bain and Burgers paths at high pressure were added when previous iterations gave unsatisfactory results for these tests. Re-tuning of algorithm inputs and/or error weights often accompanies this refinement.

A global optimization scheme combining a genetic algorithm (GA) with a local downhill optimizer provides a method for determining the spline parameters of the potential. At each iteration of the GA all potentials in the population of ten are locally optimized with 60 steps of

a Powell⁴⁸ conjugate direction algorithm, then the population is sorted and bred according to total weighted least-squares error. For the presented potential forces, stresses and energies are given weights of equal magnitude in the least-squares error. Units employed are eV/Å, eV/Å³ and eV respectively.

Breeding is done by a stochastic combination of spline knots from two parent potentials. The following constraints are enforced by introducing a “punishment” error when not satisfied: (i) $|\max[f(r)]| = |\max[p(r)]| = 1$ and (ii) n_i lies within the domain of $U(n)$ for all i . If the latter constraint is violated, the embedding function is evaluated at its nearest endpoint. At each GA step, for every potential in the population, there is a 10% chance for the embedding function domain and total density (Eq. 2) to be rescaled by a transformation where $U(n) \rightarrow U(n/\alpha)$ and $n \rightarrow \alpha n$, where α is determined by the minimum and maximum densities at the current step. When this occurs, additional gauge symmetries in the three-body terms of Eqs. 1 and 2 are exploited so that the maximal knot values of $|f|$ and $|p|$ are equal to 1.

While forces and energies are invariant with respect to these transformations, the total error is not because constraints (i) and (ii) are always satisfied after rescaling. Because during fitting the embedding function is not extrapolated but rather evaluated at the nearest endpoint when densities lie outside the domain, energies for such configurations are not invariant under the aforementioned rescaling. Furthermore, spline functions are in general not invariant under such a transformation of their argument. Thus, performing this rescaling serves as a genetic mutation of the potential. The algorithm is exited when between successive steps the change in total error for every potential in the population is less than 10^{-3} . Parameters for the fitted potential and plots of the seven functions are presented in the Supplementary Information, along with more detailed descriptions of the algorithms used. Henceforth all references to MEAM will pertain to the present empirically extended potential.

III. ACCURACY OF THE FITTED POTENTIAL

We demonstrate the accuracy of the fitted MEAM potential through the energetics of non-equilibrium structures, crystallographic defects, thermodynamic properties and phonon dispersion. All MEAM calculations in this work (other than those necessary for fitting) are performed in the Large-scale Atomic/Molecular Massively Parallel Simulator (LAMMPS)⁴⁹. Compatibility of the module has been verified for LAMMPS versions as recent as 17 November, 2016. If at any step during an MD run the density seen by an atom exceeds the embedding function domain, the embedding energy is linearly extrapolated from the nearest endpoint.

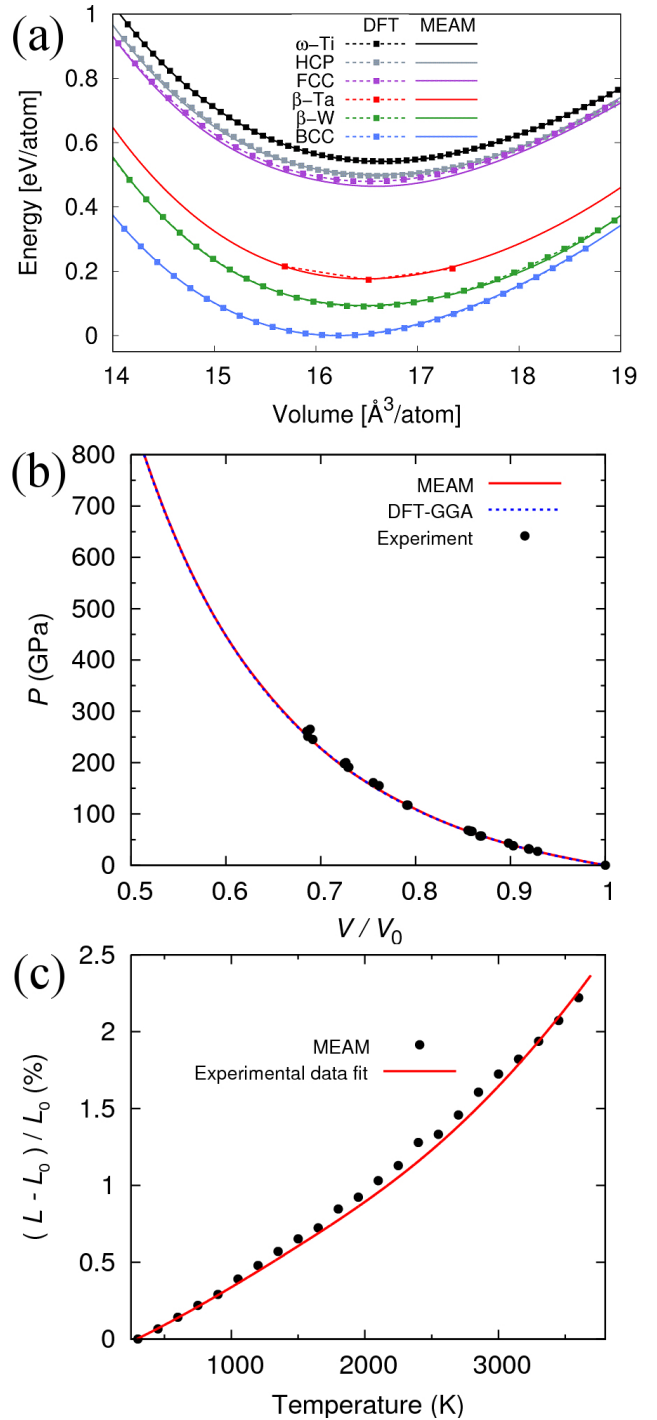


FIG. 1. (a) Comparison of energy-volume curves between MEAM and DFT for six crystal structures. Curves are ordered vertically according to the key. Our empirical potential reproduces the energies of each phase relative to that of the bcc ground state. (b) Pressure-volume relation for tungsten as computed by MEAM and DFT at 0 K compared with data from shock experiments⁵⁰ at room temperature. MEAM shows agreement with both experimental and *ab-initio* results, even at extreme pressures. (c) Thermal expansion of tungsten predicted by MEAM agrees with experimental data fit⁵¹ up to the melting point of 3695 K.

TABLE I. Zero-pressure elastic constants of bcc tungsten in GPa.

	B	C_{11}	C_{12}	C_{44}
MEAM ^a	319	550	204	147
GGA ^a	304	513	199	142
F-S ^b	309	520	204	161
LDA ^c	320	552	204	149
F-S ^d	310	525	203	159
F-S ^e	310	522	204	161
EAM ^f	308	520	202	159
BOP ^g	310	522	204	161
Expt. ^h	308–314	501–521	199–207	151–160

^aMEAM and GGA-DFT results of this work.

^bFinnis-Sinclair results of Wang *et al.*¹⁷

^cLDA-DFT results of Einarsdotter *et al.*⁵⁷

^dFinnis-Sinclair results of Derlet *et al.*¹⁵

^eFinnis-Sinclair results of Ackland *et al.*¹¹

^fEAM results of Zhou *et al.*¹⁴

^gBond-order potential results of Mrovec *et al.*¹⁶

^hExpt. results of Bolef *et al.* from 77 to 500 K⁵⁸

A. Energetics and elastic properties

Figure 1(a) shows the GGA-DFT and MEAM energy-volume relations for six distinct phases including A15 β -W and high-energy close-packed structures. MEAM accurately predicts energies of all six phases relative to the ground state. An equilibrium bcc lattice constant of 3.189 Å is predicted by both GGA-DFT and MEAM, compared to the published experimental values between 3.15 and 3.165 Å^{52–54}. It is well known now that GGA tends to overestimate the lattice constant of metals; the reason for this is discussed in Wang *et al.*⁵⁵ as well as Favot and Dal Corso⁵⁶ and references therein.

Figure 1(b) compares bcc tungsten pressure-volume relations as computed with MEAM, GGA-DFT, and measured through shock experiments⁵⁰. MEAM and GGA-DFT curves, obtained by static calculations of volumetric strain, are indistinguishable for pressures through 800 GPa and in excellent agreement with experimental results up to 300 GPa, indicating applicability of the fitted MEAM potential to high-pressure physics in tungsten.

Figure 1(c) compares linear thermal expansion predictions by MEAM to experimental results⁵¹ for temperatures between 300 K and the experimental melting point of 3695 K. Constant N-P-T MD simulations of 2000 atoms at $P = 1$ atm yield the thermal-expansion curve. Each MD simulation runs for 50,000 steps with a 1 fs timestep and the lattice constant for each temperature is determined by averaging over the last 5,000 simulation steps. MEAM shows excellent agreement with experiment up to 1,000 K and remains within 1 % of the experimental fit for all temperatures considered, indicating that the potential interpolates between temperatures included in the fitting database.

Table I shows the zero-pressure bcc elastic constants

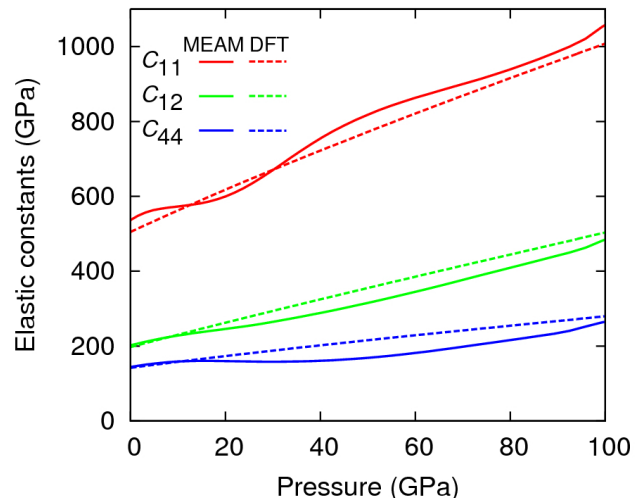


FIG. 2. Elastic constants versus pressure for bcc tungsten as computed with GGA-DFT and the fitted potential. MEAM produces elastic constants within 21% of the DFT values for all pressures shown.

of the present MEAM and GGA-DFT results, compared to previous *ab initio* calculations and other interatomic potentials. The bulk modulus B and C_{11} predicted by MEAM are higher than experimental and GGA results but consistent with the LDA work of Einarsdotter *et al.*⁵⁷. The pressure-dependence of bcc elastic constants is shown in Figure 2; MEAM does not predict a monotonic increase of C_{ij} but remains within 21 % of the GGA-DFT values.

Figure 3 shows phonon dispersion of equilibrium bcc tungsten as computed with MEAM and DFT, compared to inelastic neutron scattering results of Chen and Brockhouse⁵⁹. Dispersions are calculated using the finite-displacement method in a $7 \times 7 \times 7$ primitive bcc supercell. DFT dispersion agrees well with experiment but exhibits oscillations in the longitudinal (low-lying) branch near the H -point, a feature also found in density-functional perturbation theory results within LDA-DFT⁵⁷. Overall MEAM tracks both DFT and experiment but underestimates the frequency along the $L[\xi\xi\xi]$ branch, particularly near the ω mode at $\xi = \frac{2}{3}$.

B. Point and planar defects

Table II lists the energies of vacancies and self-interstitial atoms (SIAs) in bcc tungsten, essential quantities for the accurate modeling of plasticity. Present MEAM and DFT calculations use a $5 \times 5 \times 5$ cubic supercell. Atomic positions are relaxed to 0.01 eV. Geometric details of bcc SIA calculations can be found in Xu and Moriarty⁶². GGA-DFT calculations of Becquart *et al.*⁶⁰ and the present work indicate the $\langle 111 \rangle$ -dumbbell to be the most energetically-favorable self-interstitial, as do the present MEAM potential and F-S

TABLE II. Table of vacancy and self-interstitial formation energies (in eV) for bcc tungsten. Entries with angle-brackets indicate that the defect in question relaxes to the dumbbell configuration shown.

Defect	MEAM ^a	GGA ^a	F-S ^b	GGA ^c	F-S ^d	F-S ^e	EAM ^f	GGA ^g
Vac. Formation	2.99	3.17	3.58	3.11	3.56	3.63	3.57	3.56
Vac. Migration	1.73 [†]	1.70 [†]	1.43	1.66	2.07	1.44	2.98 [†]	1.78
Vac. Activation	4.72 [†]	4.87 [†]	5.01	4.77	5.63	5.07	6.55 [†]	5.34
$\langle 001 \rangle$ Dumbell	11.15	$\langle 111 \rangle$	11.53	11.74	11.51	9.82	12.20	11.49
$\langle 011 \rangle$ Dumbell	9.98	10.64	9.86	10.10	9.84	9.64	9.704	9.84
$\langle 111 \rangle$ Dumbell	9.73	10.31	9.58	9.82	9.55	9.82	10.56	9.55
Octahedral	11.76	12.42	11.72	11.99	11.71	10.02	12.03	11.68
Tetrahedral	10.54	$\langle 111 \rangle$	10.93	11.64	11.00	10.00	$\langle 011 \rangle$	11.05

[†]Unrelaxed calculation by present authors.

^aMEAM and GGA-DFT results of this work.

^bFinnis-Sinclair results of Wang *et al.*¹⁷

^cGGA-DFT results of Becquart *et al.*⁶⁰

^dFinnis-Sinclair results of Derlet *et al.*¹⁵

^eFinnis-Sinclair results of Ackland *et al.*¹¹

^fEAM results of Zhou *et al.*¹⁴

^gGGA-DFT results of Nguyen-Manh *et al.*⁶¹

potentials of Derlet¹⁵ and Ackland¹¹. Experiments^{63,64} and previous MD studies¹⁴ found the $\langle 011 \rangle$ -dumbell to be the favored self-interstitial structure in tungsten, but recent work⁶⁵ combining the object kinetic monte carlo (OKMC) method with dislocation loop measurements found OKMC simulations of $\langle 111 \rangle$ interstitials and 1D migration best match experiment. Vacancy formation and migration energies predicted by MEAM compare favorably with present *ab-initio* results and those of Becquart and Domain⁶⁰ while existing F-S and EAM tungsten potentials are in closer agreement with GGA results of Nguyen-Manh *et al.*⁶¹.

Figure 4 presents unrelaxed vacancy migration pathways at five equally-spaced pressures between 0 and 100 GPa. Calculations are performed using a 127-atom $4 \times 4 \times 4$ cubic bcc supercell with migration in the $\langle 111 \rangle$ direction. Overall MEAM tracks well with the DFT results; minor discrepancies are found when the vacancy lies near the lattice site and halfway between two lattice sites.

Figure 5 shows unrelaxed generalized stacking fault

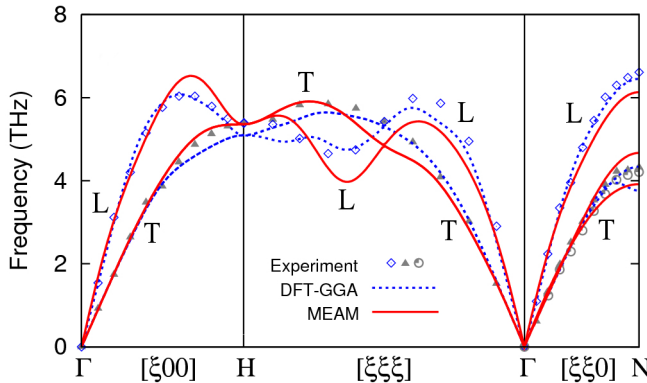


FIG. 3. Phonon dispersion for bcc W at zero pressure as calculated by DFT and MEAM, compared with inelastic neutron scattering data of Chen and Brockhouse⁵⁹.

energies (GSFEs) at five pressures on the $\{112\}$ and $\{110\}$ planes as a function of relative displacement along $\langle 111 \rangle$ for MEAM and DFT. While bcc metals are less prone to stacking-fault formation than their close-packed counterparts, they have been observed in Fe, Nb, W and Mo-35%Re to exist on $\{112\}$ and $\{110\}$ planes, formed by the dissociation of $\frac{1}{2}\langle 111 \rangle$ dislocations⁶⁶. Relaxed GSFE curves, computed with MEAM at zero pressure, do not predict the presence of any metastable stacking fault configurations. At all pressures, MEAM agrees with DFT to within a few meV/Å², and thus should be suitable for studying the effect pressure on $\{112\}\langle 111 \rangle$ and $\{110\}\langle 111 \rangle$ slip systems.

Table III shows energies and interplanar relaxations of low-index free surfaces. Present calculations employ 48-atom supercells, replicated along the surface normal with an equally-sized vacuum region and periodic

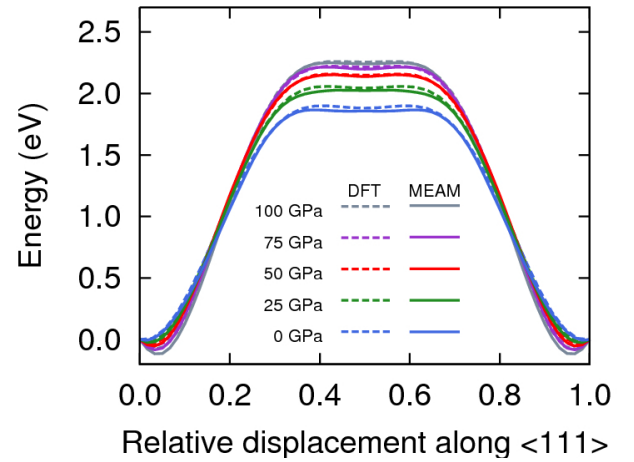


FIG. 4. Vacancy migration pathway as calculated in GGA-DFT and MEAM at multiple pressures. The shallow local minimum at $\langle \frac{1}{2} \frac{1}{2} \frac{1}{2} \rangle$ is predicted by both DFT and MEAM to increase between 0 and 100 GPa, though this effect is non-monotonic in MEAM.

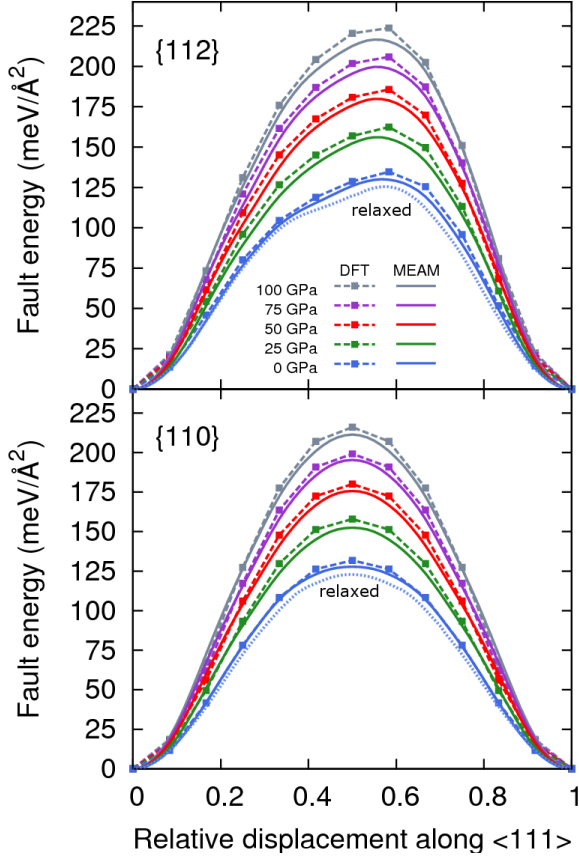


FIG. 5. Unrelaxed low-index generalized stacking fault energies (GSFE) for bcc tungsten. MEAM accurately models the evolution of both $\{110\}$ and $\{112\}$ faults with pressure. Relaxed GSFE curves computed with MEAM are shown as dotted lines for 0 GPa. Relaxation lowers fault energy slightly but does not result in any metastable configurations.

boundary conditions. All results presented here predict the $\langle 011 \rangle$ surface to have the lowest energy, followed by $\langle 111 \rangle$. Finnis-Sinclair potentials^{11,17} tend to underestimate the surface energy with respect to GGA-DFT. The present MEAM potential compares favorably with present *ab-initio* results and those of Vitos *et al.*⁶⁷ but underestimates the inter-planar relaxation of the high-energy $\langle 100 \rangle$ surface by 50%. The origin of the discrepancy between GGA-DFT results of Moitra *et al.* and the others is unclear.

Figure 6 presents the unrelaxed ideal shear stresses and energy barriers for pressures up to 100 GPa. Ideal shear defines the upper limit of stress required to deform a perfect crystal and is fundamental to our current understanding of the strength of materials. Calculations are performed following the methodology of Paxton *et al.*⁷¹, which uses a bcc primitive cell. MEAM accurately reproduces the GGA-DFT results for all pressures, with small discrepancies in shear stress around the extrema.

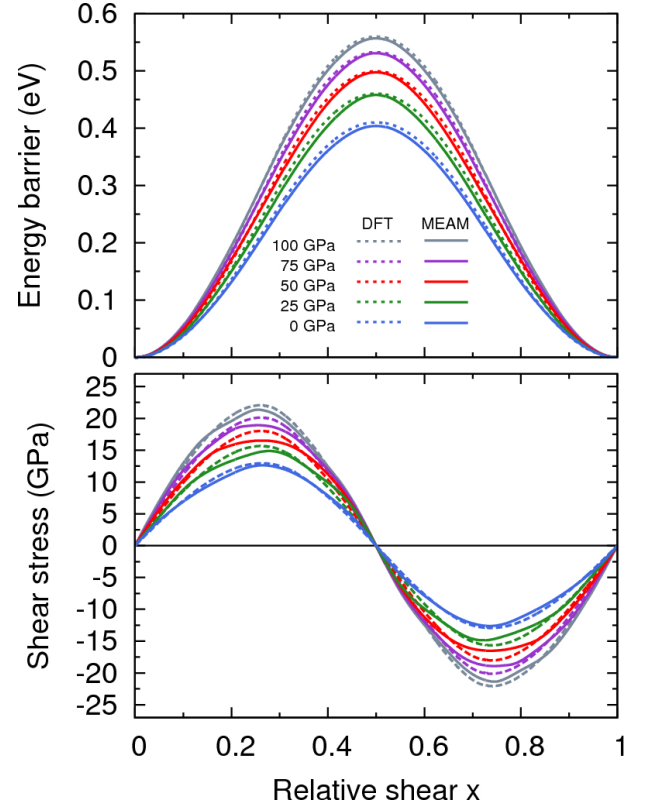


FIG. 6. Ideal shear energy (top) and stress (bottom) for a continuous deformation of a one-atom bcc unit cell corresponding to $(112)[\bar{1}\bar{1}1]$ twinning system as described by Paxton *et al.*⁷¹. MEAM Accurately reproduces the energy barrier and shear stress of this deformation for pressures up to 100 GPa. Small discrepancies in shear stress are found at the inflection points of the energy barrier, which correspond to the two extrema of shear stress at $x = 0.25$ and $x = 0.75$.

IV. TRANSFERABILITY OF THE FITTED POTENTIAL

Transferability of the fitted potential is demonstrated by application to screw dislocation core structure, deformation twinning in a bicrystal nanorod, and the high-pressure bcc-to-fcc phase transformation.

A. Dislocation core and deformation twinning

Core structure of the $\frac{1}{2}\langle 111 \rangle$ screw dislocation is determined using a cell with lattice directions $[1\bar{2}1]$, $[\bar{1}01]$, $[111]$ and periodic boundary conditions along the dislocation line. The first two lattice vectors are repeated to form a large cell containing 92,277 atoms which are displaced according to the appropriate elastic strain field. The core structure is then determined by relaxing a central region containing 54,396 atoms while the remaining atoms are fixed, ensuring that the correct boundary conditions are satisfied by the long-range anisotropic solution. This methodology is further explained in this

TABLE III. Energy and structural relaxation of low-index free surfaces in bcc tungsten. Surface energies E are given in $\text{meV}/\text{\AA}^2$ and the changes Δ_{12} in inter-planar spacing between the first two planes of the surface, where available, are given in units of percent.

	MEAM ^a	GGA ^a	F-S ^b	GGA ^c	F-S ^e	GGA ^f	AMEAM ^f	BOP ^g	MEAM ^h	Expt. ^{i,j}
E_{001}	233	245	186	289	183	487	373	237	243	—
Δ_{12}^{001}	-5.7	-11.5	-0.9	—	-0.7	—	—	-2.5	-3.2	—
E_{011}	198	200	159	249	161	398	353	163	214	—
Δ_{12}^{011}	-3.8	-3.8	-1.1	—	-0.5	—	—	-1.0	-3.0	—
E_{111}	204	216	—	278	—	449	314	—	271	—
Δ_{12}^{111}	-18.9	-21.6	—	—	—	—	—	—	-13.2	—
E_{poly}	—	—	—	—	—	—	—	—	—	187 ⁱ , 216 ^j

^aMEAM and GGA-DFT results of this work.

^bFinnis-Sinclair results of Wang *et al.*¹⁷

^cGGA-DFT results of Vitos *et al.*⁶⁷

^dFinnis-Sinclair results of Derlet *et al.*¹⁵

^eFinnis-Sinclair results of Ackland *et al.*¹¹

^fGGA-DFT and AMEAM results of Moitra *et al.*⁶⁸

^gBond-order potential results of Mrovec *et al.*¹⁶

^h2NN-MEAM results of Lee *et al.*¹³

ⁱEstimation by liquid-surface tension at 0 K, Tyson *et al.*⁶⁹

^jEstimation by atomization enthalpy at RT, Mezey *et al.*⁷⁰

group's previous work on Nb²⁹ and Mo³⁰.

Figure 7 shows a non-degenerate symmetric core structure predicted by MEAM, presented as a differential displacement map⁷², is in agreement with results from an existing bond-order potential¹⁶ and DFT-GGA⁷³ calculation for tungsten. Existing F-S potentials predict an asymmetric core^{74,75}. Our potential is also consistent with the criterion of Duesbery and Vitek⁷⁶, which is based on F-S calculations and states that the $\frac{1}{2}\langle 111 \rangle$ screw dislocation in bcc metals will have a symmetric core structure if $\gamma_{\{110\}}(b/3) > 2\gamma_{\{110\}}(b/6)$, where $\gamma_{\{110\}}$ is the relaxed $\{110\}$ γ -surface and $b = a\sqrt{3}/2$ is the burgers vector magnitude. Relaxed values taken from Figure 5 for MEAM are $\gamma_{\{110\}}(b/3) = 100 \text{ meV}/\text{\AA}^2$ and $\gamma_{\{110\}}(b/6) = 39 \text{ meV}/\text{\AA}^2$.

While dislocation slip is fundamental to plastic deformation of bulk transition metals, twinning has been found to dominate deformation in nanocrystalline Mo, Ta and Fe⁷⁷. A recent study³ observed deformation twinning and detwinning during uniaxial loading and unloading of a bicrystal nanorod. The Finnis-Sinclair potential of Ackland and Thetford¹¹ was used to model this twinning and detwinning in good agreement with experiment. We simulate this deformation as a challenge for our fitted MEAM potential and to demonstrate transferability to non-equilibrium conditions and consistency with existing models.

Figure 8 displays cross-sections of a bicrystal tungsten nanorod under uniaxial stress at 300 K. The nanorod is 128 \AA in diameter and 510 \AA in length, with periodic boundary conditions parallel to the rod axis. A compressive strain of 10 % is applied from the top of the rod over 20 ps while atomic positions are updated using the Velocity Verlet⁷⁸ integrator and canonical ensemble with 1 fs timestep. The strain is then unloaded over an additional 20 ps. Multiple $\{112\}\langle 111 \rangle$ deformation twins can be seen in Figure 8(a) through (c) to nucleate at the grain boundary and grow with increasing stress. At full loading,

strain is accommodated primarily by a single large deformation twin extending from the grain boundary to the rod surface. During unloading the accumulated strain is released by detwinning as can be seen in panels (d) through (f). This deformation behavior is nearly identical to the results of Wang *et al.*³, indicating the transferability of the fitted MEAM potential to modelling tungsten nanostructures and consistency with the successes of previously published potentials^{3,11}. Given that the F-S potential of Ackland and Thetford predicts an asymmetric core structure but accurately describes nanorod deformation³, our current MEAM potential is well suited to study the interplay of deformation twinning and dislocation-induced plasticity in tungsten.

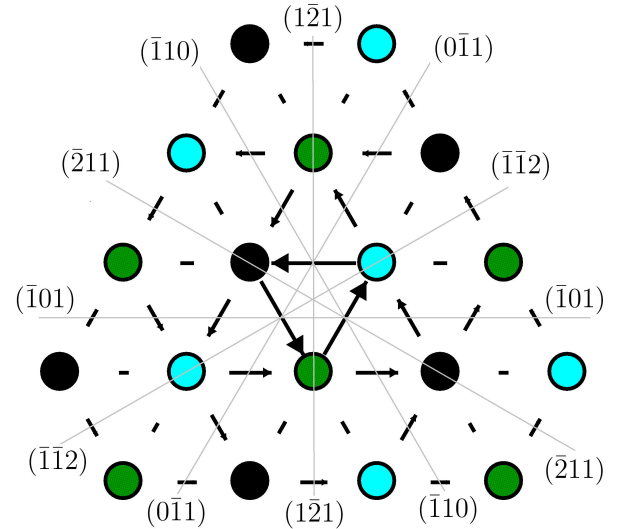


FIG. 7. Differential displacement map of the $\frac{1}{2}\langle 111 \rangle$ screw dislocation. MEAM predicts a non-degenerate symmetric core structure consistent with previous bond-order¹⁶ and GGA-DFT⁷³ calculations, whereas existing F-S potentials for tungsten predict a degenerate core⁷⁵.

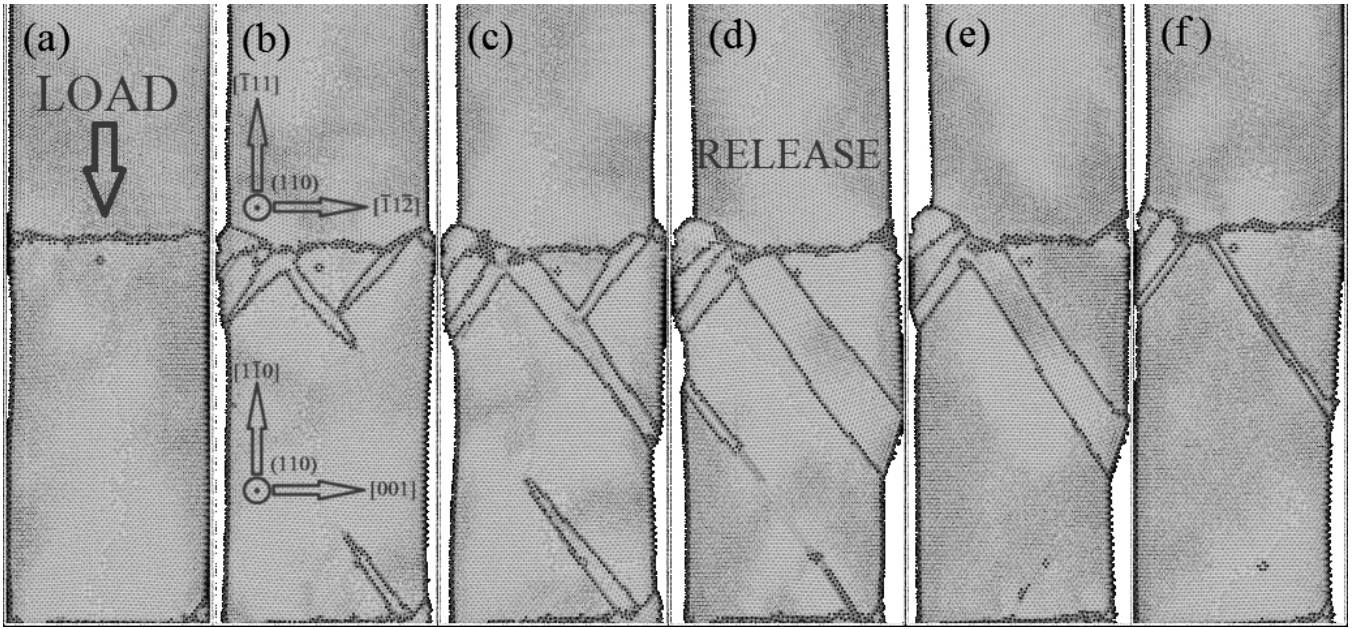


FIG. 8. Deformation twinning and detwinning in a tungsten bicrystal nanowire under axial compression at room temperature. Compare to work of Wang *et al.*³. Structure identification was performed using adaptive common neighbor analysis as implemented in OVITO^{79,80}. Atoms are color-coded by structure: light (bcc) and dark (none). (a,b,c) Multiple deformation twins of the $\{112\}\{111\}$ type grow and merge as the rod is compressed by 10%. (d,e,f) Detwinning occurs as the load is released, recovering the compressive strain. Different shades of gray appear in the bulk because of atomic-level shading in OVITO.

B. Stabilization of fcc tungsten

Finally, we investigate the stabilization of fcc tungsten at high pressure. Theoretical studies have predicted that bcc tungsten becomes thermodynamically unstable with respect to close-packed fcc and hcp phases at extreme pressures⁵⁷ and under the conditions of strong electronic excitation during laser irradiation⁸¹, for which a T_e -dependent interatomic potential was developed to study the transition¹⁸. To the authors' knowledge, fcc tungsten has only been observed in thin films formed by sputter deposition between 200 and 400 °C on glass, mica and rock-salt substrates⁸. The predicted zero-pressure lattice constants of fcc tungsten for MEAM and DFT are 4.049 Å and 4.044 Å, respectively, while Chopra *et al.*⁸ found an fcc lattice constant of 4.13 Å in the aforementioned tungsten films. Here we consider the stabilization of fcc at high pressures, some accessible via diamond-anvil experiments.

Figure 9(a) compares MEAM phonon dispersions for bcc W at pressures of 30 to 1200 GPa with LDA-DFT results of Einarsdotter *et al.*⁵⁷. MEAM force constants are computed using the small-displacement method, implemented in the Atomic Simulation Environment⁸², on a $10 \times 10 \times 10$ supercell with $\delta = a(P)/100$ where $a(P)$ is the cubic lattice constant at pressure P . LDA-DFT results employed the density-functional linear response method, norm-conserving pseudopotentials, and $5s5p5d6s6p$ valence. As seen in Figure 3, MEAM predicts the $L-\frac{2}{3}[111]$ (ω) phonon to have lower frequency

compared with DFT and experiment. This mode softens with increasing pressure, albeit at a lower rate than predicted by LDA calculations. Otherwise MEAM accurately captures the other important features of bcc dispersion up to 1200 GPa. Low-pressure results (30-60 GPa) also compare favorably with the AMEAM results of Zhang and Chen⁸³.

Figure 9(b) compares the fcc phonon dispersion predicted by MEAM and LDA-DFT at pressures from 0 to 1200 GPa. At low pressure, where fcc is a highly unfavorable structure, MEAM does not compare well to *ab initio* results but correctly predicts unstable soft modes in the $T[\xi\xi 0]$ and $T[\xi\xi\xi]$ branches. However, the stabilization of these modes with increasing pressure is non-monotonic and particularly anomalous on the $T[\xi\xi\xi]$ branch at intermediate pressures. By 1200 GPa, MEAM predicts fcc tungsten to be dynamically stable and shows excellent agreement with the LDA-DFT dispersion.

Figure 10(a) shows the elastic moduli C_{44} and C' between 400 and 500 GPa, where all C_{ij} are positive definite. It can be seen that $C' = \frac{1}{2}(C_{11} - C_{12})$ is negative for pressures below 455 GPa, reflecting the slope of the $T_{[110]}[\xi\xi 0]$ branch arbitrarily close to the Γ -point. Figure 10(b) shows this mode for pressures around 540 GPa, where long-wavelength modes are stable but the $\xi = 0.40$ mode remains unstable. According to MEAM, this mode is the last unstable phonon in any of the considered high-symmetry lines in the Brillouin zone and stabilizes at 543 GPa. However Figure 10(c), which dis-

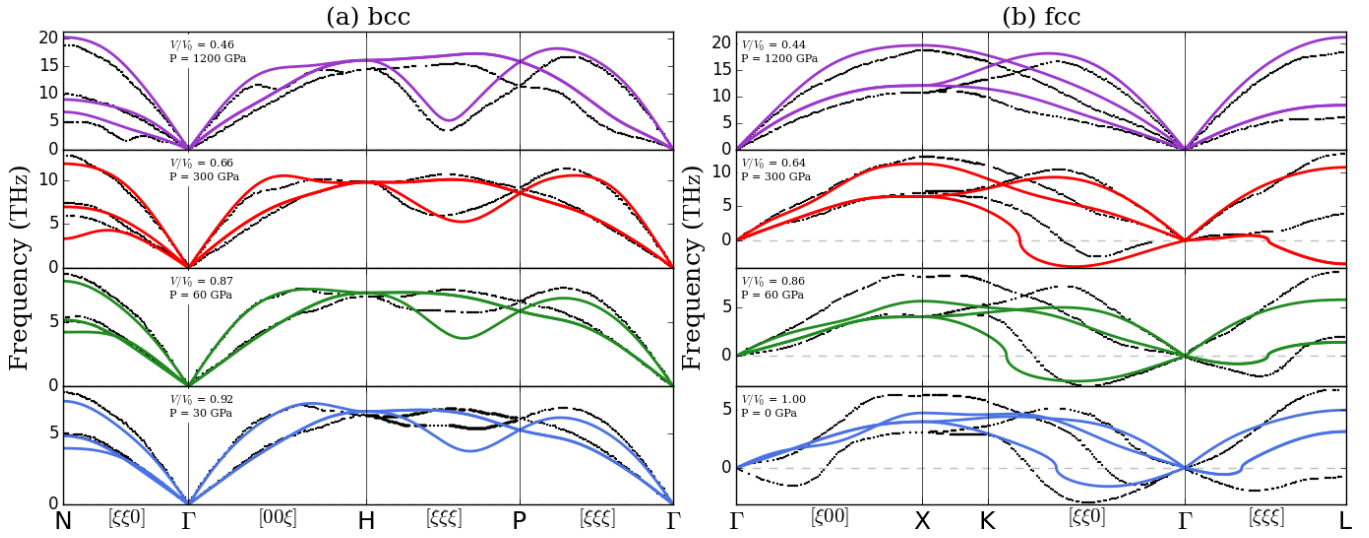


FIG. 9. MEAM (solid) Phonon dispersions at various pressures compared with LDA-DFT (dashed) work of Einarsdotter *et al.*⁵⁷ (a) bcc: MEAM is consistent with DFT even at the extreme pressure of 1200 GPa, but underestimates softening rate of the $L_{-3/2}[111]$ (ω) phonon and predicts an anomalous softening of the $T_{-1/2}[110]$ phonon with increasing pressure. (b) fcc: with the exception of the soft $T_{-1/2}[\xi\xi 0]$ and $T_{-1/2}[\xi\xi\xi]$ modes, MEAM dispersion at zero pressure diverges considerably from that of DFT. MEAM also underestimates the rate of stabilization of the soft modes with respect to DFT work. However at extreme pressures where fcc is thermodynamically stable, MEAM dispersion agrees closely with that of DFT. Displayed pressures are computed with MEAM. These dispersions were calculated using the small displacement method as implemented in the Atomic Simulation Environment⁸². As usual for phonons, negative values represent imaginary frequencies.

plays the enthalpy difference $\Delta H = H_{fcc} - H_{bcc}$ versus pressure, shows that the bcc phase remains energetically favorable until about 762 GPa. The inset in figure 10(c) shows the isobaric tetragonal Bain path at the determined pressure, displaying a barrier for the bcc→fcc transition of 140 meV/atom. This barrier persists even above 2 TPa, but accuracy of the fitted potential in this pressure range has not been verified and any further investigation should be carefully checked with first-principles methods.

To summarize, present MEAM results are consistent with LDA-DFT predictions of Einarsdotter *et al.*⁵⁷ in that for fcc C_{44} is stable at relatively low pressures, C' stabilizes before fcc is thermodynamically favorable, the last phonon mode to become real is the $T_{[110]}[\xi\xi 0]$ mode at $\xi \approx 0.4$, and that bcc remains energetically favorable until about 726 GPa. Even above this pressure there exists an energy barrier on the tetragonal bain path from bcc to fcc, again consistent with Einarsdotter *et al.*, which persists at all pressures considered here. The fitted potential should be suitable for further study of high-pressure fcc tungsten and its possible transition from the bcc phase, but predictions in the multi-TPa range should be checked with first-principles.

V. CONCLUSION

We have developed and applied a novel semi-empirical interatomic potential for tungsten, based on the MEAM and SW formalisms, parameterized using bias-free quintic splines and force-matched to a large

database of highly-converged DFT data using an evolutionary global optimization scheme. We have demonstrated accuracy of the fit by reproducing phonon frequencies, compression and thermal-expansion curves, formation energies of unfavorable crystal structures, self-interstitial defects, free surfaces, vacancies, stacking faults and ideal shear at multiple pressures. Transferability of the fitted potential has been demonstrated by description of the high-pressure bcc to fcc phase transformation, dislocation core structure and deformation twinning and detwinning of a tungsten nanorod. Given the accurate description of both deformation twinning and dislocation structure this potential is more suitable than previous models for studying their interplay. Accuracy of elastic and vibrational properties at high pressures will enable quality shock simulations, and the combination of accurate free-surfaces and non-equilibrium crystal structures should produce reliable descriptions of tungsten nanostructures.

ACKNOWLEDGMENTS

Many of the *ab-initio* calculations in our fitting database were performed by Dr. Michael Fellerger. This work was supported by the US Department of Energy under Contract No. DE-FG02-99ER45795 and used computational resources provided by the Ohio Supercomputer Center.

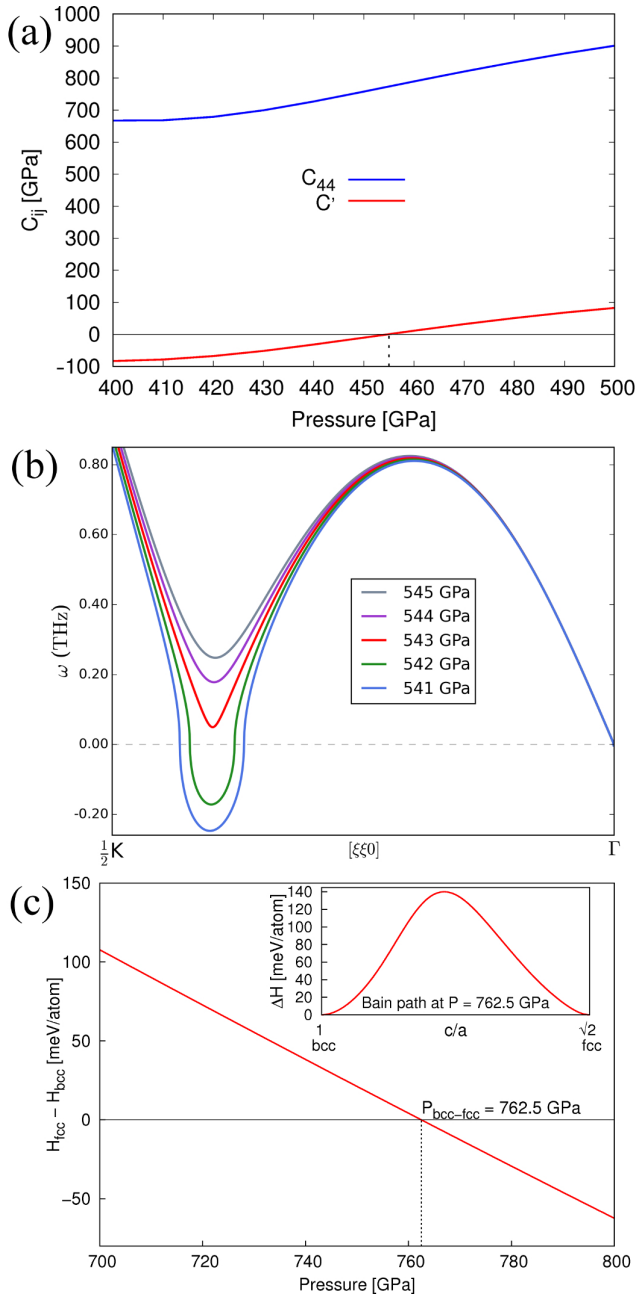


FIG. 10. Stability of fcc tungsten at 0 K. (a) shows the elastic constants C_{44} and C' as functions of pressure, demonstrating the elastic stability of fcc tungsten for pressures above 455 GPa. (b) depicts the stabilization of the fcc- $T_{[1\bar{1}0]}$ $[\xi\xi0]$ phonon branch with pressure. MEAM predicts that fcc becomes dynamically stable around 543 GPa with the $\xi = 0.4$ mode being the last to stabilize. (c) depicts the enthalpy difference $H_{fcc}(P) - H_{bcc}(P)$ between fcc and bcc as a function of pressure, revealing that despite being dynamically stable, fcc tungsten is not energetically favorable until pressures above 762.5 GPa. (inset) The tetragonal Bain path at the determined transition pressure exhibits an energy barrier of 140 meV/atom, indicating that bcc will not spontaneously transform to fcc with the fitted potential.

- ¹ T. Karabacak, A. Mallikarjunan, J. P. Singh, D. Ye, G. Wang, and T. Lu, Appl. Phys. Lett. **83**, 3096 (2003).
- ² T. Karabacak, P. Wang, G. Wang, and T. Lu, Thin Solid Films **493**, 293 (2005).
- ³ J. Wang, Z. Zeng, C. R. Weinberger, Z. Zhang, T. Zhu, and S. X. Mao, Nat. Mat. **14**, 594 (2015).
- ⁴ E. Ozawa, Y. Kawakami, and T. Seto, Scr. Mater. **44**, 2279 (2001).
- ⁵ H. Lei, Y. J. Tang, J. J. Wei, J. Li, X. B. Li, and H. L. Shi, Ultrason. Sonochem. **14**, 81 (2007).
- ⁶ Y. Shibuta and T. Suzuki, J. Chem. Phys. **129**, 144102 (2008).
- ⁷ S. S. Harilal, N. Farid, A. Hassanein, and V. M. Kozhevnikov, J. Appl. Phys. **114**, 203302 (2013).
- ⁸ K. L. Chopra, M. R. Randlett, and R. H. Duff, Phil. Mag. **16**, 261 (1967).
- ⁹ A. M. Haghiri-Gosnet, F. R. Ladan, C. Mayeux, H. Launois, and M. C. Joncour, J. Vac. Sci. Technol. A **6**, 2663 (1989).
- ¹⁰ I. A. Weerasekera, S. I. Shah, D. V. Baxter, and K. M. Unruh, Appl. Phys. Lett. **64**, 3231 (1994).
- ¹¹ G. J. Ackland and R. Thetford, Phil. Mag. A **56**, 15 (1987).
- ¹² M. I. Baskes, Phys. Rev. B **46**, 2727 (1992).
- ¹³ B. J. Lee, M. I. Baskes, H. Kim, and Y. K. Cho, Phys. Rev. B **64**, 184102 (2001).
- ¹⁴ X. W. Zhou, R. A. Johnson, and H. N. G. Wadley, Phys. Rev. B **69**, 144113 (2004).
- ¹⁵ P. M. Derlet, D. Nguyen-Manh, and S. L. Dudarev, Phys. Rev. B **76**, 054107 (2007).
- ¹⁶ M. Mrovec, R. Gröger, A. G. Bailey, D. Nguyen-Manh, C. Elsässer, and V. Vitek, Phys. Rev. B **75**, 104119 (2007).
- ¹⁷ J. Wang, Y. L. Zhou, M. Li, and Q. Hou, Modell. Simul. Mater. Sci. Eng. **22**, 015004 (2014).
- ¹⁸ S. T. Murphy, S. L. Daraszewicz, Y. Giret, M. Watkins, A. L. Shluger, K. Tanimura, and D. M. Duffy, Phys. Rev. B **92**, 134110 (2015).
- ¹⁹ F. Ercolessi and J. B. Adams, Europhys. Lett. **26**, 583 (1994).
- ²⁰ F. H. Stillinger and T. A. Weber, Phys. Rev. B **31**, 5262 (1985).
- ²¹ M. S. Daw and M. I. Baskes, Phys. Rev. B **29**, 6443 (1984).
- ²² M. S. Daw, S. M. Foiles, and M. I. Baskes, Mater. Sci. Rep. **9**, 7 (1993).
- ²³ M. I. Baskes, Phys. Rev. Lett. **59**, 2666 (1987).
- ²⁴ M. I. Baskes, J. S. Nelson, and A. F. Wright, Phys. Rev. B **40**, 6085 (1989).
- ²⁵ T. J. Lenosky, B. Sadigh, E. Alonso, V. V. Bulatov, T. D. de la Rubia, J. Kim, A. F. Voter, and J. D. Kress, Modelling Simul. Mater. Sci. Eng. **8**, 825 (2000).
- ²⁶ B. Lee, Calphad **31**, 95 (2007).
- ²⁷ Y. Mishin, D. Farkas, M. J. Mel, and D. A. Papaconstantopoulos, Phys. Rev. B **59**, 3393 (1999).
- ²⁸ R. G. Hennig, T. J. Lenosky, D. R. Trinkle, S. P. Rudin, and J. W. Wilkins, Phys. Rev. B **78**, 054121 (2008).
- ²⁹ M. R. Fellinger, H. Park, and J. W. Wilkins, Phys. Rev. B **81**, 144119 (2010).
- ³⁰ H. Park, M. R. Fellinger, T. J. Lenosky, W. W. Tipton, D. R. Trinkle, S. P. Rudin, C. Woodward, J. W. Wilkins, and R. G. Hennig, Phys. Rev. B **85**, 214121 (2012).
- ³¹ R. F. Zhang, J. Wang, I. J. Beyerlein, and T. C. Germann, Phil. Mag. **91**, 731 (2011).
- ³² R. L. C. Vink, G. T. Barkema, W. F. van der Weg, and N. Mousseau, J. Non-Cryst. Solids **282**, 2 (2001).
- ³³ Z. Jian, Z. Kaiming, and X. Xide, Phys. Rev. B **41**, 12915 (1990).
- ³⁴ F. J. Cherne, M. I. Baskes, and P. A. Deymier, Phys. Rev. B **65**, 024209 (2001).
- ³⁵ J. R. Vella, F. H. Stillinger, A. Z. Panagiotopoulos, and P. G. Debenedetti, J. Phys. Chem. B **119**, 8960 (2015).
- ³⁶ G. Kresse and J. Hafner, Phys. Rev. B **47**, 558 (1993).
- ³⁷ G. Kresse and J. Hafner, Phys. Rev. B **49**, 14251 (1994).
- ³⁸ G. Kresse and J. Furthmüller, Comput. Mater. Sci. **6**, 15 (1996).
- ³⁹ G. Kresse and J. Furthmüller, Phys. Rev. B **54**, 11169 (1996).
- ⁴⁰ P. E. Blöchl, Phys. Rev. B **50**, 17953 (1994).
- ⁴¹ J. P. Perdew, K. Burke, and M. Ernzerhof, Phys. Rev. Lett. **77**, 3865 (1996).
- ⁴² J. P. Perdew, K. Burke, and M. Ernzerhof, Phys. Rev. Lett. **78**, 1396 (1997).
- ⁴³ M. R. Fellinger, *First principles-based interatomic potentials for modeling the body-centered cubic metals V, Nb, Ta, Mo and W.*, Ph.D. thesis, The Ohio State University (2013).
- ⁴⁴ G. Kresse, J. Furthmüller, and J. Hafner, Europhys. Lett. **39**, 729 (1995).
- ⁴⁵ D. Alfé, G. D. Price, and M. J. Gillan, Phys. Rev. B **64**, 045123 (2001).
- ⁴⁶ E. Bain and N. Dunkirk, Trans. AIME **70**, 25 (1924).
- ⁴⁷ W. G. Burgers, Physica **1**, 561 (1934).
- ⁴⁸ M. J. D. Powell, Computer Journal **7**, 155 (1964).
- ⁴⁹ S. Plimpton, J. Comp. Phys. **117**, 1 (1995).
- ⁵⁰ R. Kinslow, *High-velocity impact phenomena* (Academic Press, New York, 1970) p. 522.
- ⁵¹ Y. S. Touloukian, R. K. Kirby, R. E., and P. D. Desai, *Thermophysical properties of matter: thermal expansion-metallic elements and alloys*, Vol. 12 (Plenum Press, New York, 1975).
- ⁵² W. P. Davey, Phys. Rev. **25**, 753 (1925).
- ⁵³ H. Hartmann, F. Ebert, and O. Bretschneider, Zeitschrift für Anorganische und Allgemeine Chemie **198**, 116 (1931).
- ⁵⁴ A. D. Taylor and N. J. Doyle, J. Less-Common Met. **13**, 413 (1967).
- ⁵⁵ Y. Wang, S. Curtarolo, C. Jiang, R. Arroyave, T. Wang, G. Ceder, L. Q. Chen, and Z. K. Liu, Computer Coupling of Phase Diagrams and Thermochemistry **28**, 79 (2004).
- ⁵⁶ F. Favot and A. DalCorso, Phys. Rev. B **60**, 11427 (1999).
- ⁵⁷ K. Einarsdóttir, B. Sadigh, G. Grimvall, and V. Ozolinu, Phys. Rev. B **79**, 2073 (1997).
- ⁵⁸ D. I. Bolef and J. de Klerk, J. Appl. Phys. **33**, 2311 (1962).
- ⁵⁹ S. H. Chen and B. N. Brockhouse, Solid State Commun. **2**, 73 (1964).
- ⁶⁰ C. S. Becquart and C. Domain, Nucl. Instrum. Meth. B **225**, 23 (2007).
- ⁶¹ D. Nguyen-Manh, A. P. Horsfield, and S. L. Dudarev, Phys. Rev. B **73**, 020101(R) (2006).
- ⁶² W. Xu and J. A. Moriarty, Phys. Rev. B **54**, 6941 (1996).
- ⁶³ J. A. DiCarlo, C. L. Snead, and A. N. Goland, Phys. Rev. **178**, 1059 (1969).

- ⁶⁴ S. Okuda and H. Mizubayashi, Phys. Rev. Lett. **34**, 815 (1975).
- ⁶⁵ T. Amino, K. Arakawa, and H. Mori, Sci. Rep. **6**, 26099 (2016).
- ⁶⁶ J. S. Hirschhorn, J. Less-Common Met. **5**, 493 (1963).
- ⁶⁷ L. Vitos, A. V. Ruban, H. L. Skriver, and J. Kollár, Surf. Sci. **411**, 186 (1998).
- ⁶⁸ A. Moitra, S. Kim, J. Houze, B. Jelinek, S. K. and S. Park, R. M. German, and M. F. Horstemeyer, J. Phys. D: Appl. Phys. **41**, 185406 (2008).
- ⁶⁹ W. R. Tyson and W. A. Miller, Surf. Sci. **62**, 267 (1976).
- ⁷⁰ L. Z. Mezey and J. Giber, Jpn. J. Appl. Phys. Part 1 **21**, 1569 (1982).
- ⁷¹ A. T. Paxton, P. Gumbsch, and M. Methfessel, Philos. Mag. Lett. **63**, 267 (1991).
- ⁷² V. Vitek, R. C. Perrin, and D. K. Bowen, Phil. Mag. **21**, 1049 (1970).
- ⁷³ L. Romaner, C. Ambrosch-Draxl, and R. Pippan, Phys. Rev. Lett. **104**, 195503 (2010).
- ⁷⁴ X. Tian and C. Woo, Mat. Sci. Eng. A **369**, 210 (2004).
- ⁷⁵ R. Gröger, A. G. Bailey, and V. Vitek, Acta Mater. **56**, 5401 (2008).
- ⁷⁶ M. S. Duesbery and V. Vitek, Acta Mater. **46**, 1481 (1998).
- ⁷⁷ Y. T. Zhu, X. Z. Liao, and X. L. Wu, Prog. Mat. Sci **57**, 1 (2012).
- ⁷⁸ W. C. Swope, H. C. Andersen, P. H. Berens, and K. R. Wilson, J. Chem. Phys. **76**, 637 (1982).
- ⁷⁹ A. Stukowski, Modell. Simul. Mater. Sci. Eng. **18**, 015012 (2010).
- ⁸⁰ A. Stukowski, Modell. Simul. Mater. Sci. Eng. **20**, 045021 (2012).
- ⁸¹ Y. Giret, S. L. Daraszewicz, D. M. Duffy, A. L. Shluger, and K. Tanimura, Phys. Rev. B **90**, 094103 (2014).
- ⁸² S. R. Bahn and K. W. Jacobsen, Comput. Sci. Eng. **4**, 56 (2002).
- ⁸³ X. J. Zhang and C. L. Chen, Chin. J. Phys. **51**, 359 (2013).